Effects of limestone calcination on the gasification processes in a BFB coal gasifier

L.M. Armstrong[a,], K.H. Luo[a], S. Gu[a,*]

[a] *Energy Technology Research Group, School of Engineering Sciences, University of Southampton, Southampton, SO17 1BJ, United Kingdom*

Abstract

An Eulerian-Eulerian computational fluid dynamics (CFD) model of the gasification processes in a coal bubbling fluidised bed (BFB) is presented incorporating the devolatilisation, heterogeneous, homogeneous reactions and limestone calcination. The model considers separate phases for the coal, limestone and char and is carried out for different experimental conditions taken from the literature. The results of the exiting gas compositions have been averaged over time and validated with experimental data. The hydrodynamic behaviour as well as temperature and reaction distributions within the bed are presented. The impact of limestone calcination on the gaseous composition is observed.

Key words: CFD, Gasification, Fluidised Bed, Multiphase, Limestone Calcination

---

1. Introduction

Fluidised beds technologies (FBT) offer higher efficiencies over fixed bed technologies as the fuel particles are suspended and mixed thoroughly allowing for good air-particle contact. The particles are also small so the reaction rates are fast and the good mixing allows for complete combustion of the particles to ensure that all carbon has burnt off which is an issue that occurs in fixed bed combustors with unburned carbon left amongst the ash.

---

[*] Corresponding author. Tel: +4423 8059 4760; Fax: +4423 8059 3058
Email address: `s.gu@soton.ac.uk` (S. Gu)

Preprint submitted to Chemical Engineering Journal *February 15, 2011*

Computational fluid dynamic (CFD) modelling has become a viable tool for simulating the complex gas-solid flow processes that take place in FBT. The isothermal hydrodynamics of fluidised bed reactors has attracted attention for decades to understand the complex interactions between gas and particles (Berruti et al., 1995; Samuelsberg and Hjertager, 1995; Benyahia et al., 2000; Almuttahar and Taghipour, 2008; Goldschmidt et al., 2001; Armstrong et al., 010a). Computational models predicting the heat-transfer coefficient in bubbling fluidised beds have also been carried out (Patil et al., 2006; Schmidt and Renz, 2000; Kuipers et al., 1992; Armstrong et al., 2010). The incorporation of the complex species transport equations and reactions within the coal gasification and combustion have been very limited due to the high computational cost of the models. However, the increase in computer performance and capabilities in recent years allows for such complex models to be carried out.

For hydrodynamic and heat transfer models, the Eulerian-Eulerian two-fluid model (TFM) is the most frequently applied method. The model assumes the gas and solid phases as continuous and fully interpenetrating within each control volume. It is less computationally exhaustive in comparison to the discrete Eulerian-Lagrangian method which simulates the individual particle dynamics (Gera et al., 1998, 2004; Ibsen et al., 2004) and the complete Lagrangian model which models both particles and fluid with a Lagrangian approach (Ge and Li, 1997, 2001, 2003). A combination of the Eulerian-Eulerian model and the Eulerian-Lagrangian model was recently considered by Papadikis et al. (2008, 2009a,b,c,d, 2010a,b,c,d) where one or two Lagrangian biomass particles were introduced to a Eulerian-Eulerian bubbling bed of inert sand. Although their approach is highly beneficial for the investigation at an individual particle dynamic scale, the simulation was limited to up to 5.0s in physical time. Hence, their method does not prove to be computationally viable for realistic industrial reactors which contain far more fuel particles and require simulations over a longer period to allow for the achievement of possible steady state conditions and the statistical convergence of averaged results.

The kinetic theory of granular flow (KTGF) is one of the most important tools for modelling the motion of particles. The basic concept of the kinetic theory of granular flow is the granular temperature. During random oscillations of the particles, inelastic collisions occur causing energy to be dissipated. The granular temperature measures these random oscillations of the particles and is defined as the average of the three variances of the particle's velocities. A full mathematical description of the kinetic theory is provided by Gidaspow (1994). Patil et al. (2006) carried out a comparison of the KTGF with another set of closure equations for the solid-phase rheology, namely the constant viscosity model (CVM). This model assumed the particle viscosity was constant and the particle pressure was a function of the porosity of the local solid using empirical correlations. The results found that the KTGF correctly predicted the passage of the bubble whereas the CVM showed the bubble would move away from the wall earlier.

An early comprehensive mathematical model was produced starting with simplified chemical reactions to determine emission predictions (Moreea-Taha, 2000) . However, de Souza-Santos (1989) developed what is currently regarded as a fully complete model which considered the conservation equations for the hydrodynamics including the emulsion phase and the bubbles through to the mass balance of the drying and devolatilisation processes. He considered the drying and devolatilisation processes to occur non-instantaneously whereas Chejne and Hernandez (2002) considered these processes as instantaneous since drying and devolatilisation takes place very quickly in fluidised beds. Yu et al. (2007) carried out a two-dimensional Eulerian-Eulerian model of the gasification of Colombian coal based on the experimental work of Ocampo et al. (2003). Their model included the pyrolysis, heterogeneous reactions and homogeneous reactions and produced reasonable results. Their work was further extended by Wang et al. (2009) to three-dimensions, also obtaining reasonable results. However, their model considered a single solid phase for the coal and sand which is computationally more efficient but unrealistic. As the combustion takes place, the density of the coal particles would decrease whereas the sand is inert. This should affect the flow behaviour within the bed and therefore each material should be considered a separate phase.

Limestone calcination was introduced to fluidisation modelling (FM) by de Souza-Santos (1989). Unfortunately, FMs so far do not consider the fully complex gas-particle dynamics that CFD considers however still maintains the multiphase flow dynamics with the inclusion of semi-empirical fluid-dynamic correlations for the flow behaviour in the bed. This method was also adopted by Chejne and Hernandez (2002). To the authors' knowledge, the inclusion of limestone calcination to a CFD model is yet to be carried out.

The present work introduces species and reactions models into an Eulerian two-fluid model using multiple phases. User-defined functions (UDFs) are developed for the devolatilisation model along with the kinetic and diffusion based heterogeneous reaction rates. Different experimental conditions are considered and the simulated results are compared to results given in literature. Finally, limestone calcination is introduced by means of a UDF to determine the influences calcination has on the gaseous products and subsequent reactions.

2. MODEL SETUP

The Eulerian-granular model in ANSYS 12.0 was used to model the interactions between three phases: one gaseous phase and two granular particle phases within a fluidised bed taken from the literature (Ocampo et al., 2003). This model allows for the presence of the different phases in one control volume of the grid by introducing the volume fraction variable. The solid phases, one limestone phase and one coal phase both contain spherical granular particles of the same diameter. The phases are solved individually using the mass and momentum equations. The kinetic fluctuations between particles are considered using the kinetic theory of granular flow. The virtual mass and lift effects are negligible as the lift only effects particles of large diameters and this is not the present case.

2.1. Conservation of Mass

The conservation of mass for the gaseous and solid phases are modelled using the following equations:

$$\frac{\partial\left(\alpha_g\rho_g\right)}{\partial t}+\nabla\cdot\left(\alpha_g\rho_g\vec{v}_g\right)=S_{gs} \tag{1}$$

$$\frac{\partial\left(\alpha_s\rho_s\right)}{\partial t}+\nabla\cdot\left(\alpha_s\rho_s\vec{v}_s\right)=S_{sg} \tag{2}$$

$$S_{sg}=-S_{gs}=w_i\Sigma Y_iR_i \tag{3}$$

where α_i, $\vec{v}_i$ and ρ_i represent the volume fraction, instantaneous velocity of the phase and density, respectively. A mass source term is introduced due to the mass, momentum and heat exchange between the gaseous and solid phases as a result of the heterogeneous reactions. The gas density, ρ_g, is defined as a function of species composition and temperature using the ideal gas law whilst the solid density, ρ_s, is defined by the composition of the species alone.

$$\rho_g=\frac{p}{RT\Sigma_{i=1}^{n}\frac{Y_i}{w_i}} \tag{4}$$

$$\rho_s=\frac{1}{\Sigma_{i=1}^{n}\frac{Y_i}{\rho_i}} \tag{5}$$

2.2. Conservation of Momentum

The conservation of momentum equation for the gas and solid phases are given as follows:

$$\begin{aligned}\frac{\partial\left(\alpha_g\rho_g\vec{v}_g\right)}{\partial t}+\nabla\cdot\left(\alpha_g\rho_g\left(\vec{v}_g\otimes\vec{v}_g\right)\right)&=-\alpha_g\nabla p+\nabla\cdot\overline{\overline{\tau}}_g+\alpha_g\rho_g\vec{g}\\&+K_{gs}\left(\vec{v}_g-\vec{v}_s\right)+S_{gs}\vec{v}_s\end{aligned} \tag{6}$$

$$\begin{aligned}\frac{\partial\left(\alpha_s\rho_s\vec{v}_s\right)}{\partial t}+\nabla\cdot\left(\alpha_s\rho_s\left(\vec{v}_s\otimes\vec{v}_s\right)\right)&=-\alpha_s\nabla p-\nabla p_s+\nabla\cdot\overline{\overline{\tau}}_s+\alpha_s\rho_g\vec{g}\\&+K_{gs}\left(\vec{v}_g-\vec{v}_s\right)+S_{sg}\vec{v}_s\end{aligned} \tag{7}$$

where K_{gs} and $\overline{\overline{\tau}}$ represent the interphase momentum transfer between the phases and the stress strain tensor, respectively. The stress-strain tensors for the separate phases are given by:

$$\bar{\bar{\tau}}_g = \alpha_g \mu_g \left(\nabla \vec{v}_g + \nabla \vec{v}_g^T \right) - \frac{2}{3} \alpha_g \mu_g \left(\nabla \cdot \vec{v}_g \right) \bar{\bar{I}}_g \tag{8}$$

$$\bar{\bar{\tau}}_s = \alpha_s \mu_s \left(\nabla \vec{v}_s + \nabla \vec{v}_s^T \right) + \alpha_s \left(\xi_s - \frac{2}{3} \mu_s \right) \nabla \cdot \vec{v}_s \tag{9}$$

where the bulk viscosity, ξ_s, accounts for the resistance of the particle to expansion and depression and is calculated using an expression from Lun et al. (1984). The gas viscosity, μ_g is made of the gas phase laminar viscosity and the gas phase turbulent viscosity:

$$\xi_s = \frac{4}{3} \alpha_s d_s \rho_s g_0 \left(1 + e \right) \left(\frac{\Theta_s}{\pi} \right)^{1/2} \tag{10}$$

$$\mu_g = \mu_{g_l} + \mu_{g_t} \tag{11}$$

The solid shear viscosity is composed of collisional, kinetic and frictional effects. For the collisional and kinetic effects the coefficient of restitution was introduced by Jenkins and Savage (1983) to account for the loss of energy due to particle collisions. The coefficient quantifies the elasticity of the particle collisions where a value of 0 is fully inelastic collisions whilst a coefficient of 1 is a fully elastic collisions. Schaeffer's expression (Schaeffer, 1987) is used to model the frictional viscosity in dense cases.

$$\mu_s = \mu_{s_{col}} + \mu_{s_{kin}} + \mu_{s_{fr}} \tag{12}$$

$$\mu_{s_{col}} = \frac{4}{5} \alpha_s d_s \rho_s g_0 \left(1 + e \right) \left(\frac{\Theta_s}{\pi} \right)^{1/2} \tag{13}$$

$$\mu_{s_{kin}} = \frac{10 d_s \rho_s \sqrt{\Theta_s \pi}}{96 \alpha_s \left(1 + e \right) g_0} \left[1 + \frac{4}{5} \alpha_s g_0 \left(1 + e \right) \right]^2 \tag{14}$$

$$\mu_{s_{fr}} = \frac{p_s \sin\phi}{2\sqrt{I_{2D}}} \tag{15}$$

The solids pressure considers the kinetic effects and the effects due to particle collisions and g_0 represents the radial distribution function which modifies the probability of particle collisions as the phase becomes dense:

$$p_s = \alpha_s \rho_s \Theta_s + 2 \rho_s \left(1 + e \right) \alpha_s^2 g_0 \Theta_s \tag{16}$$

$$g_0 = \left[1 - \left(\frac{\alpha_s}{\alpha_{s_{\max}}} \right)^{1/3} \right]^{-1} \tag{17}$$

The drag models simulate the interphase momentum transfer between the gas and particle phases. The Gidaspow model (Gidaspow et al., 1992) is a combination of the Wen and Yu model for dilute phases (Wen and Yu, 1966) and the Ergun model for dense phases (Ergun, 1952):

$$K_{gs} = \begin{cases} 150\,\frac{\alpha_s^2 \mu_g}{\alpha_g d_s^2} + 1.75 \frac{\alpha_s \rho_g \left|\vec{\upsilon_g} - \vec{\upsilon}_s\right|}{d_s} & \text{for } \alpha_g \leq 0.8; \\ \frac{3}{4}\, C_D\, \frac{\alpha_g \rho_g \left|\vec{\upsilon_g} - \vec{\upsilon}_s\right|}{d_s}\, \alpha_g^{-2.65} & \text{for } \alpha_g > 0.8. \end{cases} \tag{18}$$

$$C_D = \begin{cases} \frac{24}{Re_s}\left[1 + 0.15 {Re_s}^{0.687}\right] & \text{if } Re_s \leq 1000; \\ 0.44 & \text{if } Re_s > 1000. \end{cases} \tag{19}$$

$$Re_s = \frac{\rho_g \alpha_g d_s \left|\vec{\upsilon_g} - \vec{\upsilon}_s\right|}{\mu_g} \tag{20}$$

The interphase exchange coefficient between the two solid phases, namely limestone, s_1, and coal, s_2, was derived by Syamlal and O'Brien (1987):

$$K_{s_1 s_2} = \frac{3\,(1+e)\left(\frac{\pi}{2}\right) \alpha_{s_1} \alpha_{s_2} \rho_{s_1} \rho_{s_2} \left(d_{s_1} + d_{s_2}\right)^2 g_0}{2\pi \left(\rho_{s_1} d_{s_1}^3 + \rho_{s_2} d_{s_2}^3\right)} \left|\vec{\upsilon_{s_1}} - \vec{\upsilon}_{s_2}\right| \tag{21}$$

2.3. Gas Turbulence Model

The $\kappa{-}\varepsilon$ turbulence model is used to model the gaseous phase only. The solid phases are considered laminar due to the influence of drag in the bubbling bed dominating the solid flow behaviour. The turbulent mixing rate and chemical kinetic rates are calculated for the finite-rate/eddy-dissipation homogeneous reaction model therefore it is important to consider a turbulent model for the gas phase. The transport equations for κ and ε are as follows:

$$\frac{\partial\left(\alpha_g \rho_g \kappa\right)}{\partial t} + \nabla\cdot\left(\alpha_g \rho_g \vec{\upsilon_g} \kappa\right) = \nabla \cdot \alpha_g \left(\mu_{gl} + \frac{\mu_{g_t}}{\sigma_\kappa} \nabla \cdot \kappa\right) + \alpha_g G_\kappa - \alpha_g \rho_g \varepsilon \tag{22}$$

$$\frac{\partial\left(\alpha_g \rho_g \epsilon\right)}{\partial t} + \nabla\cdot\left(\alpha_g \rho_g \vec{\upsilon_g} \varepsilon\right) = \nabla \cdot \alpha_g \left(\mu_{g_l} + \frac{\mu_{g_t}}{\sigma_\varepsilon} \nabla \cdot \varepsilon\right) + \frac{\alpha_g \varepsilon}{\kappa}\left(C_{\varepsilon_1} G_\kappa - C_{\varepsilon_2} \rho_g \varepsilon\right) \tag{23}$$

$$\mu_{g_t} = \rho_g C_\mu \frac{\kappa^2}{\varepsilon} \tag{24}$$

Equation 24 defines the turbulence viscosity used in Eqn. 9. The model constants are $C_{\varepsilon_1} = 1.44$, $C_{\varepsilon_2} = 1.92$ and $C_\mu = 0.09$. The turbulent Prandtl numbers for κ and ε are $\sigma_\kappa = 1.0$ and $\sigma_\varepsilon = 1.3$, respectively. G_κ represents the generation of turbulent kinetic energy due to the mean velocity gradients and is represented by:

$$G_\kappa = \mu_{g_t} \nabla \vec{v_g} \cdot \left[\nabla \vec{v_g} + \left(\nabla \vec{v_g} \right)^T \right] - \frac{2}{3} \nabla \vec{v_g} \left(\mu_{g_t} \nabla \vec{v_g} + \rho_g \kappa \right) \tag{25}$$

2.4. Kinetic Theory of Granular Flow

The granular temperature of the solid phases is proportional to the kinetic energy of the random fluctuating motion of the particles. The following equation is solved for the granular temperature:

$$\begin{aligned} \frac{3}{2} \left[\frac{\partial}{\partial t} \left(\alpha_s \rho_s \Theta_s \right) + \nabla \cdot \left(\alpha_s \rho_s \vec{v}_s \Theta_s \right) \right] = \left(-p_s \cdot \overline{\overline{I}} + \overline{\overline{\tau}}_s \right) : \nabla \vec{v}_s - \gamma_{\Theta_s} \\ + \nabla \cdot \left(k_{\Theta_s} \cdot \nabla \Theta_s \right) - 3 K_{gs} \Theta_s \end{aligned} \tag{26}$$

The diffusion coefficient and collisional dissipation are given by:

$$k_{\Theta_s} = \frac{150 \rho_s d_s \sqrt{\Theta_s \pi}}{384 \left(1 + e \right) g_0} \left[1 + \frac{6}{5} \alpha_s g_0 \left(1 + e \right) \right]^2 + 2 \alpha_s^2 \rho_s d_s \left(1 + e \right) g_0 \sqrt{\frac{\Theta_s}{\pi}} \tag{27}$$

$$\gamma_{\Theta_s} = \frac{12 \left(1 - e \right)^2 g_0}{d_s \sqrt{\pi}} \alpha_s^2 \rho_s \Theta_s^{3/2} \tag{28}$$

2.5. Conservation of Energy

The conservation of energy considers the heat transfer within each phase and the exchange of heat between different phases. Each phase has a separate enthalpy equation and determined by the specific enthalpy, H, the mixture thermal conductivity, λ_i, and the heat exchange between the gas and solid phases,

Q_{gs}, as follows:

$$\frac{\partial}{\partial t}\left(\alpha_g\rho_g H_g\right)+\nabla\cdot\left(\alpha_g\rho_g\vec{v}_g H_g\right)=\nabla\left(\lambda_g\nabla T_g\right)+Q_{gs}+S_{gs}H_s \tag{29}$$

$$\frac{\partial}{\partial t}\left(\alpha_s\rho_s H_s\right)+\nabla\cdot\left(\alpha_s\rho_s\vec{v}_s H_s\right)=\nabla\left(\lambda_s\nabla T_s\right)+Q_{sg}+S_{sg}H_s \tag{30}$$

$$H_s=\sum_j Y_i H_i \tag{31}$$

$$H_i=\int_{T_0}^{T} C_{p,i}dT+\Delta H_{f,i} \tag{32}$$

$$\lambda_g=\sum_j\frac{X_j\lambda_j}{\Sigma_j X_j\phi_{ij}} \tag{33}$$

where H_s represents the source term that includes sources of enthalpy, H_i is the enthalpy for each species in the mixture and λ_g is the mixture thermal conductivity.

In Eqn. 33, X_i represents the molar fraction of the i^{th} species and $\phi_{ij} = \left[1+\left(\frac{\mu_i}{\mu_j}\right)^{1/2}\left(\frac{w_j}{w_i}\right)^{1/4}\right]/\left[8\left(1+\frac{w_i}{w_j}\right)\right]^{1/2}$.

The heat exchange between the phases, Q_{gs}, is an function of temperature difference and given by:

$$Q_{gs}=-Q_{sg}=h_{gs}\left(T_g-T_s\right) \tag{34}$$

An empirical relation for the interphase heat transfer coefficient between the gaseous and solid phases was proposed by Gunn (1978) which relates the Nusselt number with the particle Reynolds and the Prandtl number, $Pr=\frac{C_{p,g}\mu_g}{\kappa_g}$:

$$\begin{aligned} Nu_s=&(7-10\alpha_g+5\alpha_g^2)[1+0.7(Re_p)^{0.2}(Pr)^{1/3}]\\ &+(1.33-2.40\alpha_g+1.20\alpha_g^2)(Re_p)^{0.2}(Pr)^{1/3} \end{aligned} \tag{35}$$

2.6. Species Transport Equations

The mass fraction of each species in the phases, Y_i is determined from the conservation equation of species transport as follows:

$$\frac{\partial}{\partial t}\left(\alpha_g \rho_g Y_i\right) + \nabla\left(\alpha_g \rho_g \vec{v}_g Y_i\right) = -\nabla \cdot \alpha_g J_i + \alpha R_{g,i} + R_{s,i} \tag{36}$$

$$J_i = -\left(\rho_g D_{m,i} + \frac{\mu_t}{Sc_t}\right)\nabla Y_i \tag{37}$$

$$D_{m,i} = \frac{1 - X_i}{\Sigma_{j \neq i}\frac{X_j}{D_{i,j}}} \tag{38}$$

The second and third terms on the right hand side of Eqn. (38) represent the homogeneous rate of production of species, *i*, and the heterogeneous rate of reaction, respectively. J_i is the diffusion flux of the individual species, *i*, as a results of concentration gradients and is calculated using the modified Fick's law for the diffusion flux of chemical species in turbulent flow. Sc_t is the turbulent Schmidt number which is set to 0.7, and $D_{m,i}$ is the mixture diffusion coefficients.

2.7. Gasification Reactions

The simulation considers three separate phases, a gaseous phase and three solid phase, limestone, coal and char. The gaseous phase consists of a mixture of 8 species, namely H_2O, O_2, CO_2, CO, H_2, CH_4, Tar and N_2. As carried out by previous researcher (Petersen and Werther, 2005; Yu et al., 2007), the tar is regarded as C_6H_6 since the composition of tar is usually regarded as condensed nuclei aromatics. The limestone consists of two pseudo-species - $CaCO_3$ and CaO. When limestone calcination is considered, calcium oxide, CaO is produced which would become the active solid in the absorption of SO_4. However, due to the low amount of sulphur and nitrogen within the coal, the present model does not account for their presence in the chemical processes. Therefore only limestone calcination is considered and not limestone desulphurisation. During the devolatilisation process, the coal phase immediately transfers the char into

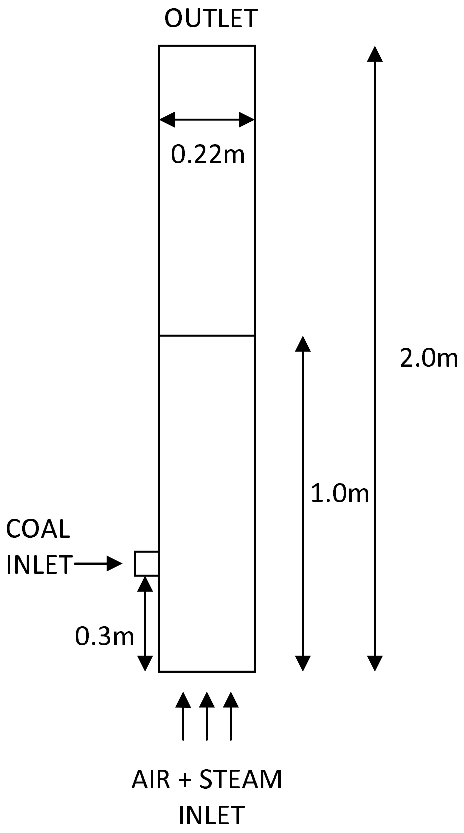

Figure 1: Experimental setup of the reactor.

the char phase whilst the gaseous volatiles are released.

$$\text{Coal} \rightarrow \text{H}_2\text{O} + \text{Volatile} + \text{Char} + \text{Ash} \tag{39}$$

$$\text{Volatile} \rightarrow a_1\text{CO}_2 + a_2\text{CO} + a_3\text{CH}_4 + a_4\text{H}_2 + a_5\text{H}_2\text{O} + a_6\text{Tar} \tag{40}$$

The yield of the volatile products released by pyrolysis is determined using the correlations derived by Loison and Chauvin (1964) which estimated the important gaseous products by the proximate analysis given in Table 2 and considered as follows:

$$Y_{\mathrm{CO_2}} = 0.135 - 0.900Y_{\mathrm{volatile(daf)}} + 1.906Y^2_{\mathrm{volatile(daf)}} \tag{41}$$

$$Y_{\mathrm{CO}} = 0.428 - 2.653Y_{\mathrm{volatile(daf)}} + 4.845Y^2_{\mathrm{volatile(daf)}} \tag{42}$$

$$Y_{\mathrm{CH_4}} = 0.201 - 0.469Y_{\mathrm{volatile(daf)}} + 0.241Y^2_{\mathrm{volatile(daf)}} \tag{43}$$

$$Y_{\mathrm{H_2}} = 0.157 - 0.868Y_{\mathrm{volatile(daf)}} + 1.388Y^2_{\mathrm{volatile(daf)}} \tag{44}$$

$$Y_{\mathrm{H_2O}} = 0.409 - 2.389Y_{\mathrm{volatile(daf)}} + 4.554Y^2_{\mathrm{volatile(daf)}} \tag{45}$$

$$Y_{\mathrm{Tar}} = -0.325 + 7.279Y_{\mathrm{volatile(daf)}} - 12.880Y^2_{\mathrm{volatile(daf)}} \tag{46}$$

The chemical processes that take place in the simulation of the coal gasification include 1) coal devolatilisation modelling; 2) hetergeous char reactions and 3) homogeneous gaseous reactions.

2.7.1. Devolatilisation Model:

The Kobayashi two-equation method proposed by Kobayashi (1976) instantaneously handles the devolatilisation of coal and volatiles release.

$$\mathrm{Coal} \overset{k_1}{\rightarrow} (1 - Z_1)\, S_1 + Z_1 V_1 \tag{47}$$

$$\mathrm{Coal} \overset{k_2}{\rightarrow} (1 - Z_2)\, S_2 + Z_2 V_2 \tag{48}$$

$$k_i = A_i \exp\left(\frac{-E_i}{RT_p}\right) \tag{49}$$

S_i represents the char that is unreacted, V_i is the volatile produced and the yield factors are given by Z_i. Kobayashi (1976) recommends that Z_1 be set to the fraction of volatiles determined by the proximate analysis as it represents devolatilisation at lower temperatures. Z_2 should be set close to unity as it is the yield of volatiles at high temperatures. The rate constants k_1 and k_2 are given in Arrhenius form where A_1 =2x10^5 s^{-1}, A_2 =1.3x10^7 s^{-1}, E_1 =1.046x10^8 J/kgmol, E_2 =1.67x10^8 J/kgmol, $Z_1 = 0.418$ and $Z_2 = 1.0$.

2.7.2. Heterogeneous Reactions:

Heterogeneous reactions take place between the char and the surrounding gases. The char combustion between the char and O_2 takes place very quickly.

The reactions take place on the external surface of the particles therefore models have been created that consider the kinetic and the diffusive rate constants as follows:

$$R_C = \left((K_{Arr})^{-1} + (K_{Dif})^{-1} \right) C_{O_2} \tag{50}$$

$$K_{Arr} = AT_s^n exp\left(\frac{E}{RT_s} \right) \tag{51}$$

$$K_{Dif} = \frac{ShD_{gs}w_C}{RT_s d_s} \tag{52}$$

$$Sh = 2.0 + 0.6Re^{1/2}Pr^{1/3} \tag{53}$$

$$D_{gs} = \frac{8.34x10^{-6}T^{1.75}}{p} \tag{54}$$

where Sh and D_{gs} are the Sherwood number and diffusion coefficient for the gas. The gasification heterogeneous reactions take place much slower than the combustion reaction and have a longer residence time within the bed. As a result, the reaction is not limited to only the external surface of the particle therefore the consideration of diffusion through the external surface does not need to be considered:

$$R_C = K_{Arr}[C_g] \tag{55}$$

The kinetic rate constants ($kgm^{-3}s^{-1}$) are taken from the literature (Ross and Davidson, 1982; Hobbs et al., 1992) and are provided in Table 1.

2.7.3. Homogeneous Reactions:

The homogeneous reactions within the gaseous phase considers the effects of turbulent flow and chemical reactions. The kinetic rate constant and the turbulent mixing rate constant were calculated using the finite-rate/eddy-dissipation model within ANSYS 12. The minimum of these two rates is then taken to be the net reaction rate.

$$R_{i,r} = min\left(R_{Arr}, R_{Edd}\right) \tag{56}$$

$$R_{Arr} = k_a T^z C_A^n C_B^m \tag{57}$$

$$R_{Edd} = 4.0 v'_{i,r} w_i \rho_g \frac{\varepsilon}{\kappa} \min \left[\min_R \left(\frac{Y_R}{v'_{R,r} w_R} \right), \frac{\Sigma_P Y_P}{2\Sigma_j^N v''_{j,r} w_j} \right] \tag{58}$$

Table 1: Heterogeneous, homogeneous & calcination reactions with their kinetic rate constants

Heterogeneous Reactions	**Kinetic Rate Constants**	**Reaction**
$C + O_2 \rightarrow CO_2$	$K_{Arr_1} = 1.04x10^5 T_c \text{exp}\left(\frac{-11200}{T_c}\right)$	R1
$C + H_2O \rightarrow CO + H_2$	$K_{Arr_2} = 342 T_c \text{exp}\left(\frac{-15600}{T_c}\right)$	R2
$C + CO_2 \rightarrow 2CO$	$K_{Arr_3} = 342 T_c \text{exp}\left(\frac{-15600}{T_c}\right)$	R3
$C + 2H_2 \rightarrow CH_4$	$K_{Arr_4} = 3.42x10^{-3} \text{exp}\left(\frac{-15600}{T_c}\right)$	R4
Homogeneous Reactions		
$CO + 0.5O_2 \rightarrow CO_2$	$K_1 = 1.0x10^{15} \text{exp}\left(\frac{-16000}{T_g}\right) C_{CO} C_{O_2}^{0.5} \rho_g^{1.5}$	R5
$H_2 + 0.5O_2 \rightarrow H_2O$	$K_2 = 5.159x10^{15} \text{exp}\left(\frac{-3430}{T_g}\right) T^{-1.5} C_{H_2}^{1.5} C_{O_2} \rho_g^{2.5}$	R6
$CH_4 + 2O_2 \rightarrow 2H_2O + CO_2$	$K_3 = 3.552x10^{14} \text{exp}\left(\frac{-15700}{T_g}\right) T^{-1} C_{CH_4} C_{O_2} \rho_g^2$	R7
$CO + H_2O \Leftrightarrow H_2 + CO_2$	$K_4 = 2780 \text{exp}\left(\frac{-1510}{T_g}\right) \left[C_{CO} C_{H_2O} - \frac{C_{CO_2} C_{H_2}}{0.0265 \text{exp}\left(3968/T_g\right)}\right]$	R8
Limestone Calcination		
$CaCO_3 \rightarrow CaO + CO_2$	$K_{cal} = \frac{3.07x10^{11}}{3.336x10^7 p \text{exp}(-20269/T_l)} \text{exp}\left(\frac{-24670}{T_l}\right)$	R9

The homogeneous reactions with their kinetic rates $\left(\text{kgm}^{-3}\text{s}^{-1}\right)$(Hurt and Calo, 2001; Chejne and Hernandez, 2002) are provided in Table 1.

2.7.4. Limestone Calcination:

Limestone calcination is the breakdown of limestone, $CaCO_3$, into calcium oxide, CaO, and carbon dioxide, CO_2. The CaO is the active solid that absorbs SO_2 producing $CaSO_4$:

$$2CaO + 2SO_2 + O_2 \rightarrow 2CaSO_4$$

However, due to the low amount of sulphur within the coal, the present model does not account for its presence in the chemical processes. The reaction and the kinetic reaction rate (Pa^{-1} s^{-1})(Borgwardt, 1970; Borgwardt and Harvey, 1972; de Souza-Santos, 1989) for the limestone calcination are given in table 1.

2.8. Initial and Boundary Conditions

The model was set up according to the experimental study of Colombian coal by Ocampo et al. (2003). An initial bed of limestone and char was set to the height of 1.0m with a volume fraction of 0.48; an equal volume fraction was used for the two solid phases of 0.24 each. The solids properties, operating conditions and experimental results are given in Table 2. Figure 1 displays a sketch of the model set up used. A mesh was created using 2215 quadrilateral cells. The cells near the wall were not refined further as the purpose of the model was to capture the gasification processes within the bed and not the near wall behaviour. Boundary conditions for the gas phase were set to no-slip and for the particulate phase a tangential slip condition was imposed which was developed by Johnson and Jackson (1987). The cell size in the horizontal direction was 0.01m whilst the vertical direction was set to 0.02m creating a domain of (22x100) cells as used previously (Enwald et al., 1999; Yu et al., 2007). The region near the coal inlet was further reduced to a minimum of 0.4mm horizontally and 0.8mm vertically to correctly capture the pyrolysis characteristics near the fuel inlet.

The finite volume method was used to solve the governing equations. The coupling and correction of the velocity and pressure is carried out for multiphase flows with the Phase Coupled SIMPLE (PCSIMPLE) algorithm (Vasquez and Ivanov, 2000). The discretisation of the convective terms was carried out with the second-order upwind scheme. A time step of 1x10^{-4} was used to ensure quick convergence with a maximum of 100 iterations per time step for a period of 20.0s. The convergence criterion between two iterations was set to 1x10^{-3}.

3. Results

Figure 2 displays the volume fraction of gases for model 1 taken over a 0.50s period after steady state conditions within the reactor were achieved. Some characteristics that can be observed include the formation of bubbles along the left side of the reactor, formation of bubbles in the lower region of the bed and also the variation of bed height. The formation of bubbles up the left wall is due to the collection of gaseous products after pyrolysis has occurred near the fuel inlet on the left hand side. As the gases build up with time, the bubbles increase

Table 2: Characteristics of solids

Coal Properties			
Proximate Analysis (wt%)			
Moisture		2.6	
Volatile matter		41.8	
Fixed carbon		54.1	
Ash		1.5	
Ultimate Analysis (wt%)			
Carbon		75.3	
Hydrogen		5.4	
Oxygen		15.6	
Nitrogen		1.8	
Sulphur		0.4	
Ash		1.5	
Others	*Limestone*	*Coal*	*Char*
Mean particle size(mm)	0.60	0.62	0.60
Apparent density (kg/m^3)	2700	1250	450
High heating value (kJ/kg)		29695	

Table 3: Operating conditions and experimental results

Operating Conditions	Model 1	Model 2
Air supply (kg/h)	21.9	17.0
Steam supply (kg/h)	4.7	4.7
Coal feed (kg/h)	8.0	8.0
Air and steam temp at entrance (°C)	420	413
Temperature of reactor (°C)	855	812
Experimental results		
H_2 (%)	8.53	8.84
CO_2 (%)	19.31	18.38
N_2 (%)	60.37	61.10
CH_4 (%)	0.84	1.07
CO (%)	10.94	10.59

in size and continue to rise up through the bed. The formation of larger bubbles near the top of the bed is a result of the coalescence of smaller bubbles. It is the movement of these bubbles through the bed that enhances mixing within a bubbling fluidised bed. The bubbles formed in the lower section of the bed are small in comparison to those observed at the top of the bed. Their formation originates from the build up of the gaseous products through heterogeneous reactions. At the inlet the oxygen concentration is highest and combustion takes place immediately upon impact with the char particles in the bed. The gases form small bubbles that continue up the bed increasing in size as further reactions and coalescence take place.

Figure 3 displays the gas, limestone and char volume fractions within the bed. The gaseous bubbles can be seen in Fig 3a) to begin formation at the base of the reactor, increasing with size as the bubbles rise and coalesce. The bubble coalescing phenomenom can be seen half way up the bed where two

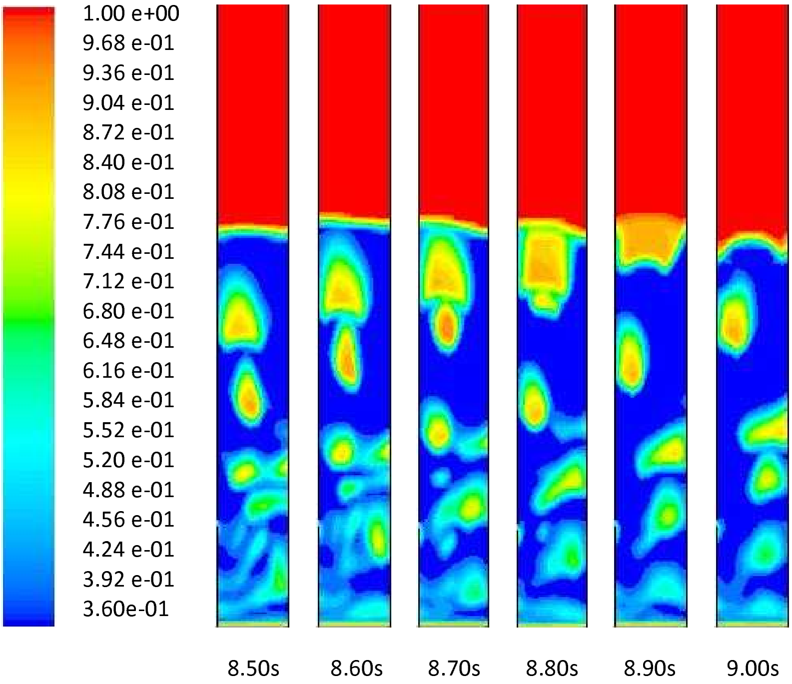

Figure 2: Gas volume fraction within the bubbling fluidised bed for model 1 over a period of 0.50s.

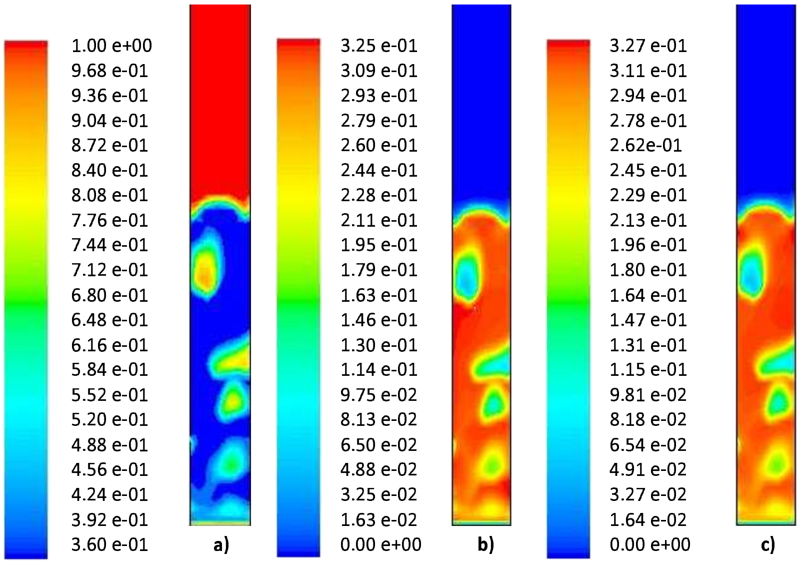

Figure 3: Volume fraction distribution within the bed for a) gases, b) limestone and c) char.

smaller bubbles are about to merge into a larger one. Also near the fuel inlet a small collection of pyrolysis products has formed and is awaiting the passage of a larger bubble from below to merge with and travel up the bed. This phenomena can be seen in the early stages of Fig 2.

The volume fraction of the limestone and char in Fig. 3b) and 3c) respectively show a similar distribution of particles within the bed. Gerber et al. (2010) displayed particle segregation of two phases with different particle diameters and the same particle densities. In this case, the particle diameters remain the same however the densities of the limestone and char differ greatly. Although no clear distinction is observed with regards to segregation in Fig. 2 close inspection indicates that the lower density particles, namely char, are segregating to the top of the bed. In order to observe these variations more effectively the relative volume fraction of the char and the limestone were compared in the bed by removing the volume fraction of char from limestone in each cell ($\alpha_l - \alpha_{ch}$). Therefore, positive values indicated a higher presence of limestone within the cell whereas negative values indicate a higher volume fraction of char. The re-

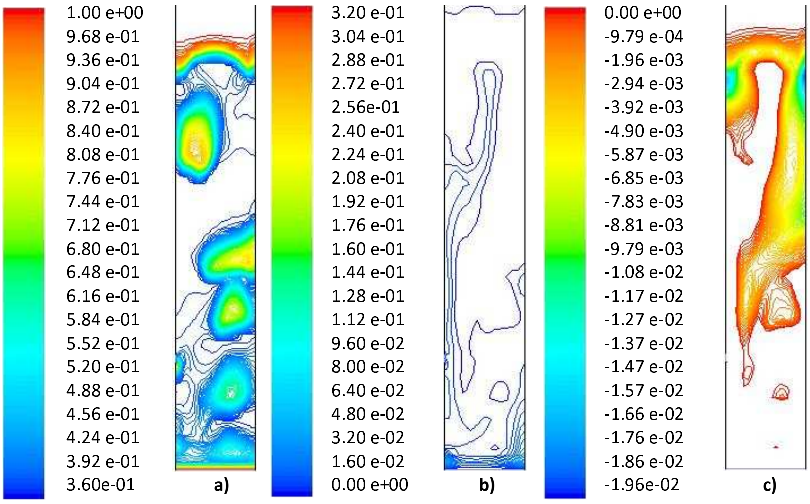

Figure 4: a) Gaseous volume fraction and the relative volume fraction distribution in the bed for b) limestone $(\alpha_l - \alpha_{ch}) > 0$ and c) char $(\alpha_l - \alpha_{ch}) < 0$.

sult for the limestone $(\alpha_l - \alpha_{ch}) > 0$ and the char $(\alpha_l - \alpha_{ch}) < 0$ are displayed in Fig. 4. The results show a collection of limestone towards the base of the bed whilst the char phase slightly dominates the centre and the top of the bed. The limestone has a higher density than the char which would result in its settlement at the base of the bed whereas the smaller char particles segregate to the top of the bed.

A higher presence of char seen in the centre of the bed can be explained by looking at the positioning of the gaseous bubbles, more obviously seen in the smaller bubbles near the base of the bed. An increased volume fraction of char within the bubbles indicates that the bubbles have a strong impact on these lower density particles compared to the higher density limestone particles. The variation in particle properties would be responsible for these slight changes as different sized particles and different densities are influenced greatly by the flow dynamics as confirmed by the different minimum fluidised velocities, i.e. $U_{mf,ch} \approx 0.055$ m/s and $U_{mf,l} \approx 0.33$ m/s, and different terminal velocities, i.e. $V_{t,ch} \approx 5.05$ m/s and $V_{t,l} = 30.3$ m/s. The ascending bubbles continually transport char particles through the bed resulting in a build up at the top of the bed. This mixing behaviour is a reason why a bubbling bed allows for excellent heating properties as the higher temperatures observed at the base of the bed, discussed further in Section 3.2, can be carried through the bed via the char particles in the bubbles.

3.1. Heterogeneous and homogeneous reactions

Figure 5 displays the reaction rates of the different heterogeneous reactions that take place in model 1. It is apparent that the mole fraction of O_2 is confined to the vicinity of the air inlet where it is immediately consumed with the combustion reaction ($C + O_2 \rightarrow CO_2$). The steam gasification reaction ($C + H_2O \rightarrow CO + H_2$) is also dominating the lower region of the bed as steam is introduced through the base of the reactor and gradually consumed. In the case of the combustion reaction, O_2 is completely consumed within the local area of the inlet.

It can be seen that the combustion reaction takes place faster than the remaining reactions. This is because the concentration of O_2 is much higher compared to the other species. As a consequence of the fast reaction rate in the vicinity of the air/steam inlet there is a fast production of CO_2. The Boudouard reaction ($C + CO_2 \rightarrow 2CO$) takes place throughout the bed but predominantly within the lower region indicating that although the combustion reaction is the dominant reaction, CO_2 as its product immediately reacts with the surrounding chars. With increasing bed height CO_2 is consumed as seen in Fig. 7b).

It can be seen in Fig. 5d) that the methanation reaction ($C + 2H_2 \rightarrow CH_4$) takes place much slower than the other heterogeneous reactions. There is a large region at the top of the bed where the methanation reaction is seen to be taking place faster. Whilst comparing Fig. 5d) with Fig. 3a) this area is a particle laden region therefore the presence of char would suggest that the steam gasification reaction could have previously dominated this region. This would also explain the low mole fraction of H_2O observed in this region in Fig. 7f), as discussed further in Section 3.3. Near the fuel inlet there appears to be a region

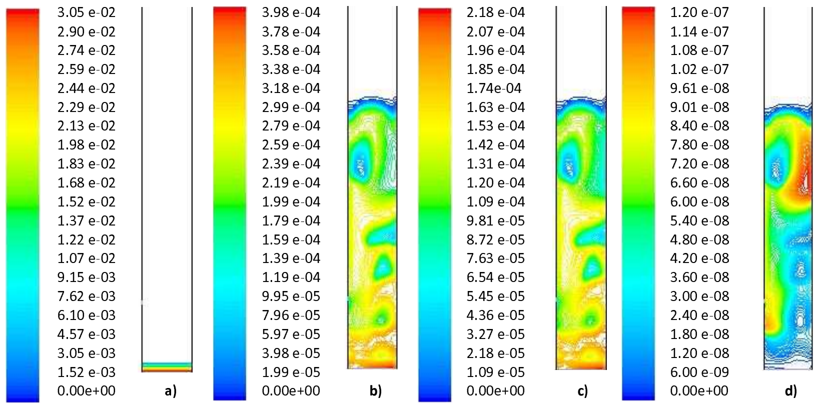

Figure 5: The reaction rates of the heterogenous reactions **a)** C - O_2, **b)** C - H_2O, **c)** C - CO_2 and **d)** C - $2H_2$.

of slightly increased rate of the methanation reaction. This could be due to the both the release of H_2 and a pyrolysis product, the gradual accumulation of H_2 as a product from the heterogeneous reaction or the water-gas shift homogeneous reaction adjusting to the increased gaseous products released within the vicinity.

The oxidation of CO, H_2 and CH_4 all take place within the vicinity of the primary inlet where the concentration of O_2 is highest. It was observed that the CO oxidation reaction took place much faster than the H_2 and CH_4 oxidation reactions due to the Boudouard reaction leading to a higher concentration of CO near the air inlet as seen in Fig. 5. The reaction rate for the CH_4 oxidation is much lower than the other homogeneous reactions as the only heterogeneous reaction that produces CH_4 is the methanation reaction which takes place extremely slowly, especially in the lower regions where there is a limited concentration of H_2.

3.2. Temperature distributions

Figures 6a) and b) display the contour plots of the gaseous temperature distribution for model 1 with two scales. In Fig. 6a) it can be clearly seen that the highest temperature is observed at the base of the reactor where the exothermic combustion reaction dominates. Figure 6b) displays a modified scale of Fig. 6

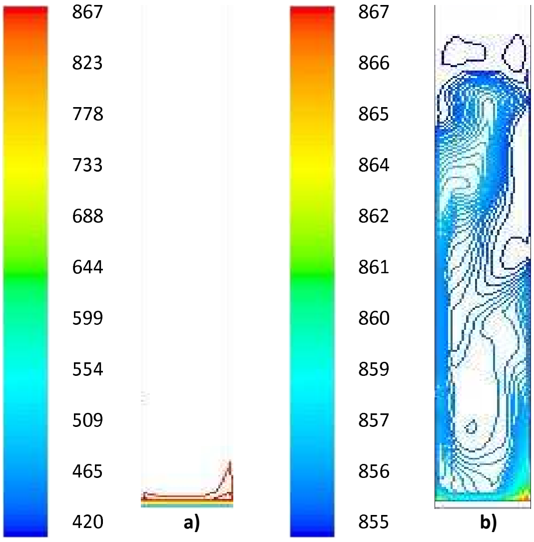

Figure 6: The gaseous temperature distribution (°C) within the reactor for model 1 **a)** with a complete scale and **b)** a modified scale to highlight the temperture distribution within the bed.

for the benefit of observing the temperature in different regions within the bed. There is a clear difference in temperature throughout the bed depending on position and local reactions. The temperatures near the wall remain similar to that of the reactor walls whilst the centre of the bed varies. A region near the top of the bed on the right hand side shows a significantly lower temperature than the remaining bed. This region was brought up previously as showing a low mole fraction of H_2O (Fig. 7f) and a significantly higher methanation reaction rate (Fig. 5d). The previous assumption was that previously this region was exerted to strong steam gasification activity. This is confirmed with the lower temperature as the steam gasification reaction and Boudouard reaction are endothermic therefore a reduction in local gaseous temperature would indicate the presence of such reactions. The methanation reaction is slightly exothermic however the methanation reaction rate in this region is significantly lower than the other heterogeneous reactions taking place in that region for it to make a significant effect.

A slight temperature increase is observed near the top of the bed on the left. It can be seen in Fig. 3a) that there is a large gaseous bubble within this region. An increase in temperature would indicate that the water-gas shift reaction is taking place within the vicinity particularly within the bubble where the endothermic heterogeneous reactions rates are lower (Fig. 5b,c). As with all the homogeneous reactions, the water-gas shift reaction is slightly exothermic therefore it highlights its influence on the temperature within this particular region.

Factors that would affect the temperature within the bed however would be the variation of thermal boundary conditions e.g. different wall temperatures and the introduction of heat transfer coefficients on the wall as carried out previously for biomass (Gerber et al., 2010). The variation in temperature within the bed would greatly affect the composition of the species as the reaction kinetics for the heterogeneous, homogeneous and pyrolysis reactions exhibit a strong dependence on the temperature. We are carrying out further simulations to confirm the effects within the coal BFBG.

3.3. Gas compositions

The gaseous mole fraction distributions within the reaction for model 1 are given in Fig. 7. There is a clear distinction between the combustion products which are more concentrated towards the base of the reactor and those which increase in concentration with increasing height. The species N_2, H_2O and CO_2 show a larger mole fraction at the base of the reactor since N_2 and H_2O are introduced through the lower air/steam inlet. The CO_2 is introduced endogenously as the product of the dominating combustion heterogeneous reaction. These gaseous species decrease with height as they are consumed by further reactions. CH_4, H_2 and CO build up in concentration with increasing height as they are the products of heterogeneous reactions and accumulate as further reactions take place.

The region near the fuel inlet shows a particularly concentrated region for

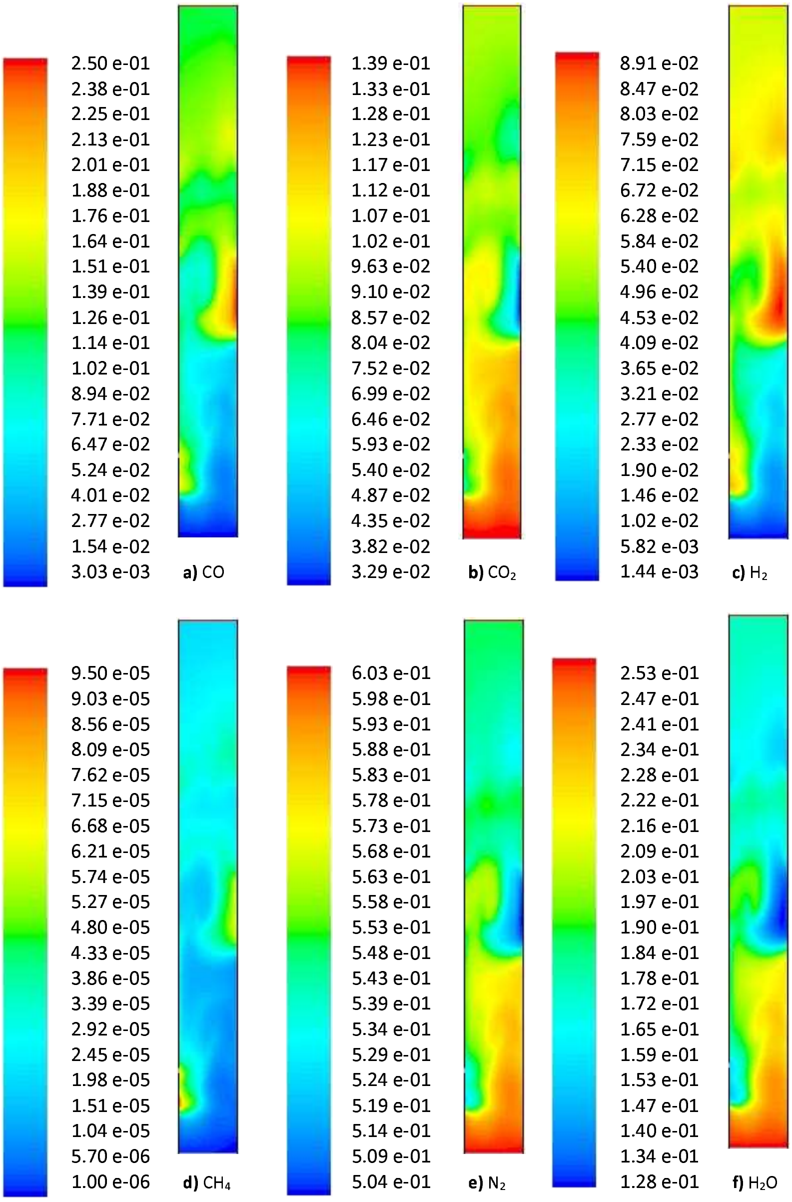

Figure 7: The mole fractions of the different gaseous products for model 1.

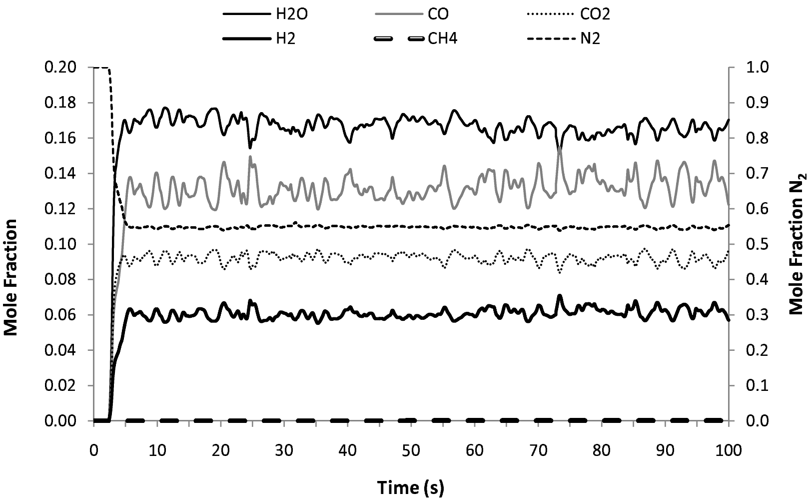

Figure 8: The average mole fraction of each gaseous product through the outlet over a period of 100.0s.

all gaseous species, except for N_2, H_2O and CO_2. This region signifies the accumlation of pyrolysis products as the fuel is entered into the bed at this point. The products then mix through the bed along with the products from the bed base region to continually trigger further reactions, i.e. heterogeneously within the bed as seen in Fig. 5 and finally with the water-gas shift which dominates above the bed.

It is apparent that the heterogeneous reactions result in a strong variation in the mole fraction within the bed since the reactions depend on the local concentrations of the species which consequently influence further reactions as increased concentrations of their products accumulate. An example of this would be the large region at the top right of the bed which, as was previously discussed, consists of a very low concentration of H_2O yet an increased mole fraction of H_2 and CO. This would also confirm the previous assumption that the steam gasification reaction had previously dominated this region leading to an increased concentration of its products. It can also be seen that the mole fraction of CH_4 is gradually increasing which agrees with Fig. 5d) where a fast methanation reaction rate can be seen.

Above the bed the mole fractions in all cases regulate as the water-gas shift reaction takes place. An ideal case would be for the water-gas shift reaction to reach equilibrium resulting in very little fluctuations in the average mole fraction of the gaseous products through the outlet as seen in Fig. 8. Whilst extensive work has been carried out with regards to the kinetics of the water-gas shift reaction it has been widely accepted that equilibrium is attainable whilst maintaining temperatures of 800-850 °C for tall large scale beds. Unfortunately, this is highly unlikely within lab-scale reactors as the freeboard is not tall enough for equilibrium to be completely achieved. This is the case seen here in model 1 (Fig. 8) as stronger fluctuations are observed for the four species involved in the water-gas shift reaction, namely H_2O, CO, CO_2 and H_2.

From as early as 5.0s the composition of the species through the outlet remains relatively steady with fluctuations occuring as the water-gas shift reaction continually compromises between the dominating species. The mole fraction of N_2 and CH_4 appears more consistant with average mole fractions of 54.7% and 0.02% respectively although CH_4 is so low that it is not as apparent in the graph. This is due to their non-participation in any of the reactions except for the methanation reaction where the reaction rate is small and would not influence greatly the variation in CH_4 fluctuations.

The fluctuations of the remaining products appear strongly correlated with the mole fraction of its species. For H_2O and CO, averages of 16.4% and 13.5%, respectively, display larger fluctuations than CO_2 and H_2. It can be seen that the fluctuations of these different groups reflect each other showing a decrease in CO whilst H_2O increases. The same can be seen for the remaining species. This is a result of the water-gas shift reaction not reaching equilibrium and the species having to compromise with an increased concentration of one of the species on each side of the reaction. We are currently running some models to determine whether this effect will be reduced with an increased freeboard area.

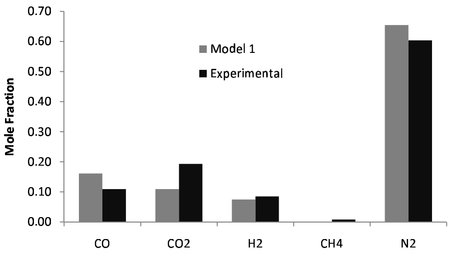

Figure 9: Average mole fraction of the exiting gaseous products for Model 1.

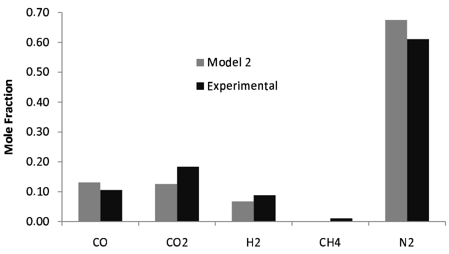

Figure 10: Average mole fraction of the exiting gaseous products for Model 2.

3.4. Comparison with experimental data

The results for the gasification models were compared to the experimental results given in the literature (Ocampo et al., 2003). The mole fraction composition of the exit gases for the inert model 1 and model 2 are given in Fig. 9 and Fig. 10. The models both provide a reasonably good representation of the experimental compositions however it can be seen, particularly in model 1, that the composition of CO is higher than that of CO_2 unlike the experimental results. This is expected as the experimental bed consisted of limestone whereas this model is formed of both char and limestone. As a result, the catalytic behaviour of the char consumed the CO_2 faster via the Boudouard reaction. Furthermore, this also agrees with the findings of Gerber et al. (2010) who carried out a parametric study on the effects of the inclusion of heat transfer coefficients with a char bed of a biomass BFBG. They found that an ideal adiabatic model, as presently used, provided a higher temperature distribution hence increasing the reaction kinetics for CO_2 consumption. The results of model 2 has an increase in CO_2 compared to that in model 1 due to the initial set up having a lower temperature distribution in the bed which would reduce the reaction kinetics for CO_2 consumption. For further comparison, the average mole fractions for model 1 and model 2 are also given in Table 4 along with the experimental results.

Model 1 and 2 were both rerun with the inclusion of limestone calcination to determine its effect on the composition of the exiting gases. The comparison

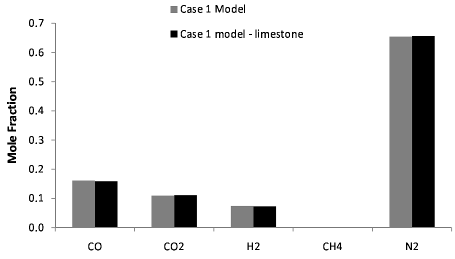

Figure 11: Average mole fraction of the exiting gaseous products for Model 1 with inert and calcinating limestone.

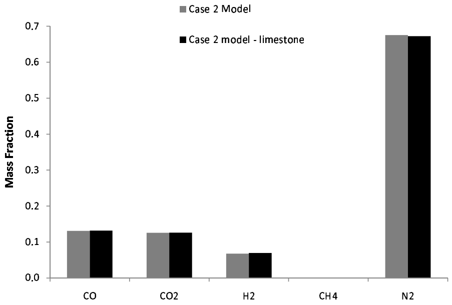

Figure 12: Average mole fraction of the exiting gaseous products for Model 2 with inert and calcinating limestone.

between an inert limestone and a calcinating limestone bed are given in Fig. 11 and Fig. 12, respectively. From these graphs there does not appear to be a great deal of variation between the compositions of the gaseous products. This is due to the slow conversion rate of limestone decomposition. Wang et al. (2007) investigated the effects of temperature and residence time on the decomposition of limestone of similar sized particles in a CO_2 atmosphere and found that with a BFB temperature of 920°C, the residence time for over 73% conversion of $CaCO_3$ to CaO was approximately 70mins. Therefore, the 100s run time presented here would not provide a great deal of CO_2 release.

Table 4 displays the average mole fractions for both model 1 and model 2 for both an inert bed and a calcinating bed. The difference between the mole fractions are also given to highlight the impact that limestone calcination has on a gaseous composition. In both cases there is a slight increase in the mole fraction of CO_2 as expected due to the release of CO_2 during limestone decomposition however the impact is different between the two models. In model 1, the results show a slight decrease in the mole fraction of CO and H_2 whilst H_2O increases with CO_2. This is similar behaviour to that displayed in Fig. 8 indicating that the limestone model impacts the water-gas shift reaction as a result of further introduction of CO_2.

Model 2 shows an increase in all species except H_2O which decreases. It can be observed that model 1 and model 2 vary significantly in H_2O due to the variation in reactor temperature. The water-gas shift reaction is dependent on temperature and gaseous concentration and since the temperature distribution of the bed remains the same between an inert bed and the calcinating bed it can be assumed that the impact would be due to a slight increase in gaseous compositions. This is plausible as a lower temperature results in a lower mole fraction of CO since the temperature dependent Boudouard reaction rate is reduced. An increase in CO_2 from the limestone helps to further promote the Boudouard reaction causing an increase in CO composition allowing for a more efficient water-gas shift reaction. Increasing the composition of the CO would accelerate the forward water-gas shift reaction leading to a reduction in H_2O and an increase in the products CO_2 and H_2. As the reaction continues the species compromise and adjust according to the local species concentration. It is interesting that the species CH_4 and tar do not vary between the inert model and a calcinating model. In addition to their low mole fraction within the bed this would be due to their non-involvement with the water-gas shift reaction.

A further point to emphasise is the use of a char and limestone bed would not display a great impact during limestone calcination and the heterogeneous reaction rates with char dominate over the limestone reactions. The authors are investigating the effects of different bed material on the gaseous compositions in an extensive parametric study.

4. Conclusion

An Eulerian-Eulerian model was carried out on a coal bubbling fluidised bed gasifier with a char and limestone bed. Furthermore, limestone calcination was introduced to determine the impact such reactions have on gaseous compositions leaving the reactor. The compositions of the gaseous species were validated with experimental data from the literature.

Hydrodynamic investigations displayed the formation of bubbles formed exogenously and endogenously as a result of the reaction kinetics. Multiple phases

Table 4: Average mole Fraction of gaseous species for an inert limestone and a calcinating limestone bed and the impact calcination has on the compositions.

Model 1	CO	CO_2	H_2	CH_4	N_2	H_2O	Tar
Inert	0.13464	0.09150	0.06226	0.00020	0.54675	0.16428	0.00037
Calcinating	0.13249	0.09279	0.06094	0.00020	0.54671	0.16649	0.00037
Difference	-0.00214	0.00130	-0.00132	0.00000	-0.00003	0.00220	0.00000
Model 2	CO	CO_2	H_2	CH_4	N_2	H_2O	Tar
Inert	0.10135	0.09742	0.05230	0.00014	0.52268	0.22584	0.00026
Calcinating	0.10268	0.09818	0.05422	0.00014	0.52379	0.22073	0.00026
Difference	0.00132	0.00076	0.00192	0.00000	0.00111	-0.00511	0.00000
Experiment	CO	CO_2	H_2	CH_4	N_2	H_2O	Tar
Exp 1	0.1094	0.1931	0.0853	0.0084	0.6037	N/A	N/A
Exp 2	0.1059	0.1838	0.0884	0.0107	0.6110	N/A	N/A

were used for the different bed phases, char and limestone, and their different material properties led to segregation as lower density char particles were seen to be transported not only through the mixing behaviour of the bed but at a higher proportion compared to limestone within the ascending bubbles. The denser limestone particles were seen to descended to the base of the reactor.

An investigation into the heterogeneous reaction showed the complete consumption of oxygen near the air/steam inlet as a result of the dominating combustion reaction. The remaining gasification heterogeneous reactions took place in different regions of the reactor depending on the local concentration of the gasifying species. H_2O and CO_2 dominated the lower region of the bed as the bed was introduced with H_2O and CO_2 was a product of the combustion reaction. Such species were shown to decrease in mole fraction with increasing height as they got consumed by further reactions. The methanation reaction took place higher in the bed after an accumulation of H_2 as a product of heterogeneous reactions and the pyrolysis process. The homogeneous oxidation reactions took place near the air/steam inlet where there was O_2 present. Higher in the bed the water-gas shift reaction took place.

The temperature distribution within the bed was presented more extensively than previous CFD models of gasification processes. As seen previously, higher temperatures were observed in the vicinity of the air/steam inlet as the exothermic combustion of oxygen took place however reducing the temperature scale displayed varying temperatures throughout the bed as a result of the different reactions taking place locally. The Boudouard and steam gasification reactions are endothermic and their presence throughout the bed at different rates resulted in temperature reductions. Furthermore, the homogeneous reactions including the water-gas shift are exothermic so in regions of low solid volume fraction, namely the bubbles, there appeared to be a slight increase in temperature as a result of the water-gas shift reaction taking place.

The mole fraction of the gaseous species were taken at the exit of the reactor over time and, as expected in lab-scale reactors, fluctuations indicated that the water-gas shift reactor had not reached equilibrium. Further work is being carried out to determine the effects of bed height on the water-gas shift reaction with the assumption that a larger freeboard provides a better opportunity for equilibrium to be achieved. The average mole fractions were compared also to experimental results for different experimental setups. Reasonable results were achieved however an increase in CO and decrease in CO_2 was observed in the models compared to experimental data. This is due to the present expansion of previous work to include char in the bed compared to only limestone in the experimental reactor. A lower mole fraction of CO_2 was observes as its reaction with a larger quantity of char took place throughout the bed increasing the mole fraction of CO as a consequence. The impact of temperature variation was also highlighted since a lower temperature resulted in a lower production of CO and higher CO_2. This was a result of the reaction kinetics being highly temperature dependent and a lower temperature led to a reduced reaction rate for the Boudouard reaction.

Limestone calcination was introduced to a computational fluid dynamic model with results showing only slight effects. One reason for this is the presence of char in the bed in the present study compared to just a bed of limestone alone in the previous work. Another reason could be the relatively short simulation time, which does not show the full effects of limestone calcination. However, slight changes were observed in the gaseous compositions due to the introduction of further CO_2 as a result of limestone decomposition. Its impact affected the water-gas shift reaction as the species adjust to reach an equilibrium. Further work is being carried out to determine the influence of inert limestone, calcinating limestone, char only and varying char/limestone ratio beds in an extensive parametric study in coal bubbling fluidised bed gasifiers.

The present basic case managed to capture the physical behaviour and predict the gaseous emissions reasonable well. This model will be extended to in future work to include parametric variations and the mass variations of the solid phases, e.g. carbon, $CaCO_3$ and CaO, over longer periods of time. Extension of this basic model to incorporate NOx and SOx modelling would be a significant advancement in the modelling of fluidised bed technologies.

Nomenclature

Greek Letters

α_i	Volume fraction
γ_i	Collisional dissipation of energy, W/mK
κ	Turbulent kinetic energy, m^2/s^2
λ_i	Thermal conductivity of species, W/m^2K
μ_i	Shear viscosity, kg/s m
ϕ	Angle of internal friction, °, Eq. (15)
ρ_i	Density, kg/m^3
σ_κ	Turbulent Prandtl numbers for κ
σ_ε	Turbulent Prandtl numbers for ε

τ_i	Stress tensor, Pa
Θ_s	Particle phase pseudo-temperature, m/s^2
υ_i	Velocity, m/s
ε	Dissipation rate of turbulent kinetic energy, m^2/s^3
ξ_i	Bulk viscosity, kg/s m

Symbols

t	Time, s
$\overline{\overline{I}}$	Stress tensor, Pa
C_D	Drag coefficient
C_i	Concentration of species i, kmol/m^3
C_p	Specific heat, J/kgK
d_s	Particle diameter, m
D_i	Diffusion coefficient for species, m^2/s
e	Coefficient of restitution
g	Gravity, m/s^2
g_0	Radial distribution function
G_κ	Shear production
H	Specific enthalpy, J/kg
h	Heat transfer coefficient, W/m^{2}K
J_i	Diffusion flux if species i, kg/m^{2}s
k_{Θ_s}	Diffusion coefficient for granular energy, kg/ms
K_{Arr}	Kinetic rate constant

K_{Dif}	Diffusion rate constant
K_i	Drag, kg/m^{3}s
p	Gas pressure, Pa
p_i	Phase pressure, Pa
Q_i	Intensity of heat exchange between phases, W/m^2
R	Universal gas constant, J/kmol K
$R_{g,i}$	Net rate of production of homogeneous species i
$R_{s,i}$	Heterogeneous reaction rate
S_i	Mass source term, kg/m^{3}s
T	Temperature, K
w_i	Species molecular weight, kg/kmol
X_i	Molar fraction of species
Y_i	Mass fraction of species

Subscripts

g	Gas phase
i	General Index, ith species
q	Phase
s	Solids phase
w	Wall
c	Char
g_l	Gas laminar flow
g_t	Gas turbulent flow

Dimensionless Numbers

Nu	Nusselt number
Pr	Prandtl number
Re	Reynolds number
$\mathrm{Sc_t}$	Turbulent Schmidt number
Sh	Sherwood number

References

F. Berruti, J. Chaouki, L. Godfroy, T. Pugsley, G. Patience, Hydrodynamics of circulating fluidized bed risers: a review., Can. J. Chem. Eng. 73(5) (1995) 579–602.

A. Samuelsberg, B. Hjertager, An experimental and numerical study of flow patterns in a circulating fluidized bed reactor., Int. J. Multiphase Flow 22 (1995) 575–591.

S. Benyahia, H. Arastoopour, T. Knowlton, H. Massah, Simulation of particles and gas flow behaviour in the riser section of a circulating fluidized bed using the kinetic theory approach for the particulate phase., Powder Technol. 112 (2000) 24–33.

A. Almuttahar, F. Taghipour, Computational fluid dynamics of high density circulating fluidized bed riser: Study of modeling parameters., Powder Technol. 185 (2008) 11–23.

M. Goldschmidt, J. Kuipers, W. van Swaaij, Hydrodynamic modelling of dense gas-fluidized beds using the kinetic theory of granular flow: effect of restitution coefficient on bed dynamics., Chem. Eng. Sci. 56 (2001) 571.

L.-M. Armstrong, K. Luo, S. Gu, Two-dimensional and three-dimensional computational studies of hydrodynamics in the transition from bubbling to circulating fluidised bed, Chem. Eng. J. 160 (2010a) 239–248.

D. Patil, J. Smit, M. van Sint Annaland, J. Kuipers, Wall-to-bed heat transfer in gas-solid bubbling fluidized beds, AIChE J. 52 (2006) 58–74.

A. Schmidt, U. Renz, Numerical prediction of heat transfer in fluidized beds by a kinetic theory of granular flows, Int J Therm Sci. 39 (2000) 871–885.

J. Kuipers, W. Prins, W. van Swaaij, Numerical calculation of wall-to-bed heat transfer coefficients in gas-fluidized beds., AIChE J. 38 (1992) 1079–1091.

L.-M. Armstrong, K. Luo, S. Gu, The influence of multiple tubes on the tube-to-bed heat transfer in a fluidised bed, In Print: Int. J. Multiphase Flow (2010).

D. Gera, M. Gautam, Y. Tsuji, T. Kawaguchi, T. Tanaka, Computer simulation of bubbles in large-particle fluidized beds., Powder Technol. 98 (1998) 3847.

D. Gera, M. Syamlal, T. O'Brien, Hydrodynamics of particle segregation in fluidized beds., Int. J. Multiphase Flow 30 (2004) 419–428.

C. Ibsen, E. Helland, B. Hjertager, T. Solberg, L. Tadrist, R. Occelli, Comparison of multifluid ans discrete particle modelling in numerical predictions of gas particle flow in circulating fluidised beds., Powder Technol. 149 (2004) 29–41.

W. Ge, J. Li, Pseudo-particle approach to hydrodynamics of gas/solid two-phase flow., in: Proceedings of the 5th International Conference on Circulating Fluidized Beds, Beijing: Science Press., pp. 260–265.

W. Ge, J. Li, Macro-scale pseudo-particle modeling for particle-fluid systems., Chin. Sci. Bulletin 46(18) (2001) 1503–1507.

W. Ge, J. Li, Macroscale phenomena reproduced in microscopic systems-pseudo-particle modeling of fluidization., Chem. Eng. Sci. 58 (2003) 1565–1585.

K. Papadikis, A. Bridgwater, S. Gu, CFD modelling of the fast pyrolysis of biomass in fluidised bed reactors, part a: Eulerian computation of momentum transport in bubbling fluidised beds, Chem. Eng. Sci. 63 (16) (2008) 4218–4227.

K. Papadikis, S. Gu, A. Bridgwater, CFD modelling of the fast pyrolysis of biomass in fluidised bed reactors. part b: Heat, momentum and mass transport in bubbling fluidised beds, Chem. Eng. Sci. 64 (2009a) 1036–1045.

K. Papadikis, H. Gerhauser, A. Bridgwater, S. Gu, CFD modelling of the fast pyrolysis of an in-flight cellulosic particle subjected to convective heat transfer, Biomass and Bioenergy 33(1) (2009b) 97–107.

K. Papadikis, S. Gu, A. Bridgwater, CFD modelling of the fast pyrolysis of biomass in fluidised bed reactors: Modelling the impact of biomass shrinkage, Chem. Eng. J 149 (2009c) 417–427.

K. Papadikis, S. Gu, A. Bridgwater, H. Gerhauser, Application of CFD to model fast pyrolysis of biomass, Fuel Processing Technology 90 (2009d) 504–512.

K. Papadikis, S. Gu, A. Bridgwater, Computational modelling of the impact of particle size to the heat transfer coefficient between biomass particles and a fluidised bed, Fuel Processing Technology 91(1) (2010a) 68–79.

K. Papadikis, A. Bridgwater, S. Gu, A CFD approach on the effect of particle size on char entrainment in bubbling fluidised bed reactors, Biomass and Bioenergy 34(1) (2010b) 21–29.

K. Papadikis, S. Gu, A. Fivga, A. Bridgwater, Numerical comparison of the drag models of granular flows applied to the fast pyrolysis of biomass, Energy and Fuels 24 (3) (2010c) 21332145.

K. Papadikis, S. Gu, A. Bridgwater, 3d simulation of the effects of sphericity on char entrainment in fluidised beds, Fuel Processing Technology (2010d).

D. Gidaspow, Multiphase flow and fluidization, continuum and kinetic theory descriptions., Academic Press, Inc., 1994.

R. Moreea-Taha, Modelling and simulation for coal gasification, in: CCC-42, ISBN 92–029-354-3, UK.

M. de Souza-Santos, Comprehensive modeling and simulation of fluidized bed boilers and gasifiers, Fuel 68 (1989) 1507–1521.

F. Chejne, J. Hernandez, Modeling and simulation of coal gasification process in fluidized bed, Fuel 81 (2002) 1687–1702.

L. Yu, J. Lu, X. Zhang, S. Zhang, Numerical simulation of the bubbling fluidized bed coal gasification by the kinetic theory of granular flow (ktgf), Fuel 86 (2007) 722–734.

A. Ocampo, E. Arenas, F. Chejne, J. Espinel, C. Londono, J. Aguirre, J. Perez, An experimental study on gasification of Colombian coal in fluidised bed, Fuel 82 (2003) 161–164.

X. Wang, B. Jin, W. Zhong, Three-dimensional simulation of fluidized bed coal gasification, Chem. Eng. Proc. 48 (2009) 695–705.

C. Lun, S. Savage, D. Jeffrey, N. Chepurniy, Kinetic theories for granular flow: Inelastic particles in Couette flow and slightly inelastic particles in a general flow field., J. Fluid Mech. 140 (1984) 223–256.

J. Jenkins, S. Savage, A theory for the rapid flow of identical, smooth, nearly elastic, spherical particles., J. Fluid Mech. 130 (1983) 187202.

D. Schaeffer, Instability in the evolution equations describing incompressible granular flow., J. Diff. Equ. 66 (1987) 19–50.

D. Gidaspow, R. Bezburuah, J. Ding, Hydrodynamics of circulating fluidized beds: Kinetic theory approach., in: Proceedings of the 7th Fluidization Conference.

Y. Wen, Y. Yu, Mechanics of fluidization., Chem. Eng. Prog. Symp. Ser. 62 (1966) 100.

S. Ergun, Fluid flow through packed columns., Chem. Eng. Prog. 48(2) (1952) 89–94.

M. Syamlal, T. O'Brien, Derivation of a drag coefficient from velocityvoidage correlation., in: U.S. Dept. of Energy, Office of Fossil Energy, National Energy Technology Laboratory, Morgantown, West Virginia April.

D. Gunn, Transfer of heat or mass to particles in fixed and fluidised beds., Int J Heat Mass Transfer 21 (1978) 467–476.

I. Petersen, J. Werther, Experimental investigation and modeling of gasification of sewage sludge in the circulating fluidized bed, Chem. Eng. Proc. 44(7) (2005) 717–736.

R. Loison, R. Chauvin, Pyrolise rapide du charbon, Chimie et Industrie 91 (1964) 269.

H. Kobayashi, Devolatilization of Pulverized Coal at High Temperatures, Ph.D. thesis, Department of Mechanical Engineering, Massachusetts Institute of Technology, Cambridge, Mass., 1976.

I. Ross, J. Davidson, The combustion of carbon particles in a fluidized bed., Chem. Eng. Res. Des. 60a (1982) 108–114.

M. Hobbs, P. Radulovic, L. Smoot, Modeling fixed-bed coal gasifiers, AIChE J. 38 (1992) 681–702.

R. Hurt, J. Calo, Semi-global intrinsic for char combustion modeling, Combustion and Flame 125 (2001) 1138–2114.

R. H. Borgwardt, Kinetics of the reaction of SO_2 with calcined limestone, Environ. Sci. Technol. 4 (1970) 59–63.

R. H. Borgwardt, R. D. Harvey, Properties of carbonate rock related to SO_2 reactivity, Environ. Sci. Technol. 6 (1972) 350–360.

P. Johnson, R. Jackson, Frictional-collisional constitutive relations for granular materials, with application to plane shearing., J. Fluid Mech. 176 (1987) 67–93.

H. Enwald, E. Peirano, A. Almstedt, B. Leckner, Simulation of the fluid dynamics of a bubbling fluidized bed experimental validation of the two-fluid model and evaluation of a parallel multiblock solver., Chem. Eng. Sci. 54 (1999) 311–328.

S. Vasquez, V. Ivanov, A phase coupled method for solving multiphase problems on unstructured meshes., in: Proceedings of ASME FEDSM'00: ASME 2000 Fluids Engineering Division Summer Meeting, Boston.

S. Gerber, F. Behrendt, M. Oevermann, An eulerian modeling approach of wood gasification in a bubbling fluidized bed reactor using char as bed material, Fuel 89(10) (2010) 2903–2917.

Y. Wang, S. Lin, Y. Suzuki, Study of limestone calcination with co_2 capture: decomposition behavior in a co_2 atmosphere, Energy and Fuels 21 (2007) 3317–3321.